An improved dynamic bidirectional coupled hydrologic-hydrodynamic model for efficient flood inundation prediction

Yanxia Shen, Zhenduo Zhu, Qi Zhou, Chunbo Jiang[*]

State Key Laboratory of Hydroscience and Engineering, Department of Hydraulic

Engineering, Tsinghua University, Beijing, 100084, China

Abstract: To improve computational efficiency while maintaining numerical accuracy, coupled hydrologic-hydrodynamic models based on non-uniform grids are used for flood inundation prediction. In those models, a hydrodynamic model using a fine grid can be applied for flood-prone areas, and a hydrologic model using a coarse grid can be used for the remaining areas. However, it is challenging to deal with the separation and interface between the two types of areas because the boundaries of the flood-prone areas are time-dependent. We present an improved Multigrid Dynamical Bidirectional Coupled hydrologic-hydrodynamic Model (IM-DBCM) with two major improvements: 1) automated non-uniform mesh generation based on the D∞ algorithm was implemented to identify the flood-prone areas where high-resolution inundation conditions are needed; 2) ghost cells and bilinear interpolation were implemented to improve numerical accuracy in interpolating variables between the coarse and fine grids. A hydrologic model, two-dimensional (2D) nonlinear reservoir model was bidirectionally coupled with a 2D hydrodynamic model that solves the shallow water equations. Three cases were considered to demonstrate the effectiveness of the improvements. In all cases, the mesh generation algorithm was shown to efficiently and successfully generate high-resolution grids in those flood-prone areas. Compared with the original M-DBCM (OM-DBCM), the new model had lower RMSEs and higher

---

[*]Corresponding author: State Key Laboratory of Hydroscience and Engineering, Department of Hydraulic Engineering, Tsinghua University, Beijing, 100084, China
Corresponding author: Tel: +8613581891886; E-mail address: jcb@tsinghua.edu.cn

24   NSEs, indicating that the proposed mesh generation and interpolation were reliable and

25   stable. It can be adapted adequately to the real-life real flood evolution process in

26   watersheds and provide practical and reliable solutions for rapid flood prediction.

27   **Key words:** Coupled hydrologic-hydrodynamic model; Multi-grid generation; Bilinear

28   interpolation; Computational efficiency and accuracy; Flood simulation

29   **1 Introduction**

30   Floods are the most frequent natural disasters that seriously harm human health

31   and economic growth. Numerical models are critical for predicting flooding processes

32   to help prevent or mitigate the damaging effects of floods on people and communities

33   (Bates, 2022). Coupled hydrologic-hydrodynamic models are widely used to translate

34   the amount of rainfall obtained from weather forecasting models or rain gauge

35   observations into surface inundation (Xia et al., 2019).

36   Coupled hydrologic-hydrodynamic models can be generally divided into external

37   (one-way) and internal (two-way) coupling models (see Figure 1). The external

38   coupling models utilize hydrographs obtained from hydrologic models as an input for

39   hydrodynamic models in a fixed position, providing a one-way transition (Schumann

40   et al., 2013; Feistl et al., 2014; Choi and Mantilla, 2015; Bhola, 2018; Wing et al., 2019).

41   It is powerful tools for watershed flood simulation, in particular large spatial and

42   temporal scale, due to its convenience in model construction. However, this one-way

43   flow information cannot capture the mutual interaction between runoff production and

44   flood inundation, and the fixed interface is inconsistent with the actual flood process

45   where the inflow discharge positions, flow path, and discharge values change with

46   accumulating rainfall.
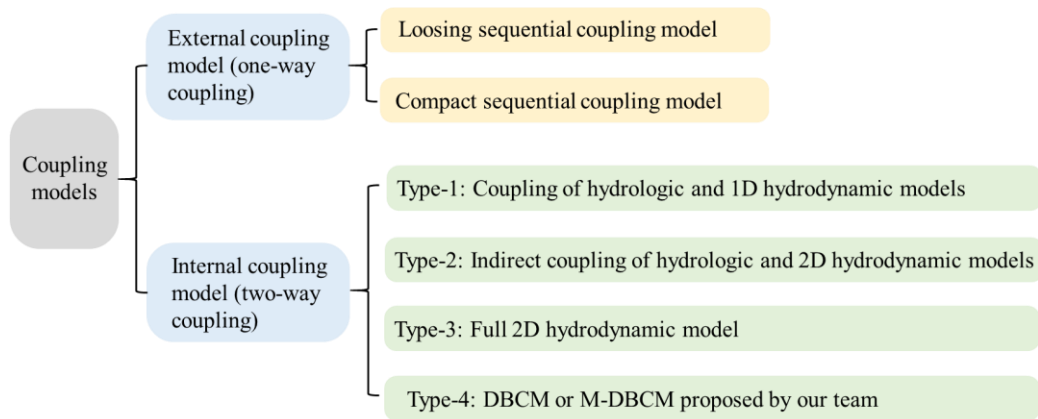
47

48   Figure 1 Classifications of coupled hydrologic and hydrodynamic models

49   The two-way coupling models are further divided into: the coupled hydrologic-1D

50   hydrodynamic model (HH1D), indirect coupled hydrologic-2D hydrodynamic models

51   (ICM2D), full 2D hydrodynamic models (HM2D), and dynamic bidirectional coupling

52   model (DBCM or M-DBCM) proposed by author's team. In the HH1D, the discharges

53   obtained from the hydrologic model is treated as mass source of the 1D hydrodynamic

54   model, while the water depth calculated in 1D hydrodynamic model is fed back to

55   hydrologic model, such as the coupled Mike SHE and Mike 11 (Thompson et al., 2004).

56   The application of 1D modeling of overland flow is limited when developing precise

57   and reliable flood maps in 2D inundation regions.

58   In order to overcome the lack of 2D hydrodynamic simulation in HH1D, the

59   ICM2D is proposed, where the runoff first flows into 1D rivers, and then discharge into

60   the 2D inundation regions (Seyoum et al., 2012; Chen et al., 2017 and 2018). For

61   example, Mike SHE and Mike11 are coupled to form Mike Urban, and Mike11 and

62   Mike21 are dynamically coupled to form Mike Flood. The indirect coupling between

63   the hydrologic and the 2D hydrodynamic models can be developed by coupling Mike

64   Urban and Mike Flood. The 1D hydrodynamic model is a connection channel between

65   the hydrologic and the 2D hydrodynamic models. Compared with the HH1D, this

66   coupling type has satisfactory and acceptable accuracy and is widely used. As the 2D

67 hydrodynamic model is only calculated in local inundation regions, its computational

68 efficiency is greatly improved in comparison with the HM2D. However, the ICM2D

69 assumed that the water first discharges into the 1D rivers, and then flows from 1D rivers

70 to the 2D regions. The hydrologic model is not directly coupled with the 2D

71 hydrodynamic model, which is inconsistent with the actual flood processes. In reality,

72 water may be discharged into both 1D channel and 2D waterbodies simultaneously, and

73 the hydrologic and 2D hydrodynamic models should be linked directly. Direct coupling

74 of hydrologic and 2D hydrodynamic models can physically reflect the flood processes,

75 which deserves more attention.

76   In HM2D, the 2D hydrodynamic model is used to simulate the overland flow

77 (runoff routing and flood inundation), and the runoff generation serves as its mass

78 source term (Singh et al., 2011; Garcia-Navarro et al., 2019; Hou et al., 2020; Costabile

79 and Costanzo, 2021). It has satisfactory and acceptable numerical accuracy and has

80 been widely used. But the development and simulation of HM2D require high-

81 resolution topographic data at the catchment scale and extensive computational time,

82 which hinder their application in large-scale flood forecasting (Kim et al., 2012). In

83 HEC-RAS (US Army Corps of Engineers, 2023), for instance, the flooding process in

84 1D rivers was simulated by a 1D hydrodynamic model, whereas the flooding process

85 in 2D regions was simulated using 2D diffusion wave equations (DWEs) or shallow

86 water equations (SWEs). If the 2D regions were discretized into finer grids and the 2D

87 SWEs was applied, the 1D hydrodynamic model was coupled with the 2D SWEs. It has

88 high numerical accuracy but is computationally prohibitive for large-scale applications.

89 Conversely, if the 2D regions were discretized into coarse grids and the 2D DWEs was

90 applied, the 1D hydrodynamic model was coupled with the 2D DWEs, which can

91 expand the application scale at the cost of reducing the accuracy.

92   Jiang et al. (2021) proposed a DBCM based on uniform structured grids, where

93   the hydrologic and 2D hydrodynamic models were coupled in a two-way manner and

94   the coupling interface of these two models was time-dependent. The model can

95   automatically evolve the surface flow and fully consider the flow states with both mass

96   and momentum transfer. However, because uniform grids were adopted in DBCM, it

97   inevitably increased the computational cost and time, especially in the large watershed.

98   An essential consideration to reduce computational time is mesh coarsening

99   (Caviedes-Voullième et al., 2012). Adaptive mesh refinement (AMR) has been used to

100   optimize the grid resolution during flood simulations (Donat et al., 2014; Hu et al., 2018;

101   Ghazizadeh, 2020; Ding et al., 2021; Kesserwani and Sharifian, 2023). Aiming to

102   increase computational efficiency by reducing computing nodes, it adjusts grid size for

103   local grid refinement by domain features or flow conditions. Yu (2019) used quadtree

104   grids to divide the computational domain and applied the DBCM to simulate the

105   flooding process. It needs to segment and merge the grid elements repeatedly during

106   the calculation, which can be time-consuming and offset the calculation time saved by

107   the optimized grid. AMR is commonly employed in scenarios where flow

108   characteristics exhibit abrupt variations, such as aerodynamic shock waves, hydraulic

109   jumps, and seismic tsunami waves. Capturing discontinuous solutions necessitates local

110   grid refinement, with the location of refinement dynamically adapting to the position

111   of the discontinuities. AMR is indispensable for this purpose. Flow characteristic

112   variations arising from abrupt geometric changes in the computational domain can be

113   captured using static local refinement grids, provided that the extent of these changes

114   is limited. This approach offers computational time savings.

115   Static non-uniform grids simplified grid generation procedure compared with

116   AMR (Caviedes-Voullième et al., 2012; Hou et al., 2018; Bomers et al., 2019; Ozgen-

117   Xian et al., 2020). Compared with uniform grids and AMR, it can not only reduce

118   computational nodes, but use different time steps in different grid sizes to further reduce

119   computation time. Shen et al. (2021) and Shen and Jiang (2023) divided the

120   computational domain based on static multi-grids, where the different grid size ratios

121   of coarse to fine grids were designed. But there were two limitations to this scheme.

122   One limitation is that the grids need to be generated manually, which can be subjective

123   and uncertain. It also needs a heavy workload, especially for large watersheds. Besides

124   the grid generation, the variable interpolation between the coarse and fine cells was also

125   not reasonable. There are shared and hanging nodes at the interpolation interface. Shen

126   et al. (2021) assumed the variables at the shared nodes were equal to that at the cell

127   center, and the hanging nodes were calculated by the shared nodes. The results showed

128   that this scheme has unsatisfactory accuracy and frequently fails to converge. Although

129   the multi-grid-based model can reduce computational time, there are remarkable

130   challenges such as the grid partition technique, determination of coarse and fine regions,

131   and variables interpolation between coarse and fine grids.

132   The objective of this study is to develop an integrated system that fully couples

133   the hydrologic and 2D hydrodynamic models, utilize an automated method for efficient

134   multi-grid mesh generation, and resolve variable interpolation between coarse and fine

135   grids more accurately. An improved dynamic bidirectional coupling model (IM-DBCM)

136   was presented, where the 2D nonlinear reservoir (NLR) model was coupled with the

137   2D hydrodynamic model through a CMI. The D∞ algorithm was implemented to divide

138   the computational domain into non-uniform grids automatically. Ghost cells (i.e., the

139   virtual cells located on the boundaries of the computational domain) and bilinear

140   interpolation were used to interpolate variables between the coarse and fine grids. Three

141   case studies were conducted, and the simulation results were compared with the original

142   M-DBCM (OM-DBCM) to evaluate the effectiveness of the improvements.

143   **2 Methodology**

144   The Fortran programming language was adopted to apply the coupling model. The

145   framework of IM-DBCM is illustrated in Figure 2. The model consists of two

146   components: a hydrologic model (i.e., 2D NLR) that simulates the runoff generation

147   and routing, and 2D hydrodynamic model simulating the flood inundation process.

148   Before the model setup, it is required to first design the grids. Static multi-grids were

149   applied to the model. For the model execution, the variables interpolation between

150   coarse and fine grids and the coupling of hydrologic and hydrodynamic models are the

151   two main issues that must be addressed.
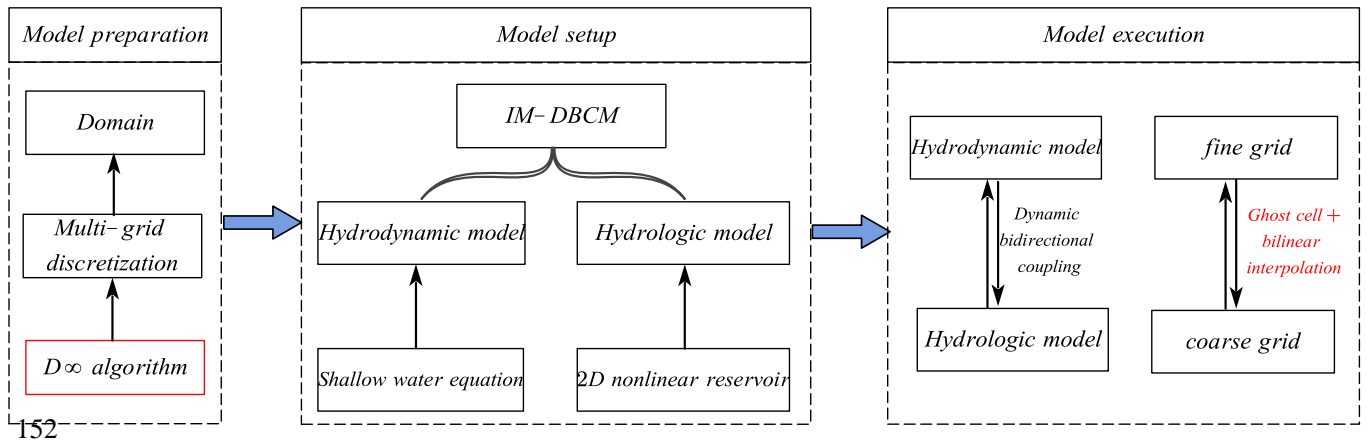
152

153   Figure 2 Framework of IM-DBCM

154   **2.1 Automated multi-grid generation**

155   Associated with flood models, the design of computational grids that are scalable

156   and suitable for all applications is challenging. The grid generation can be considered

157   as a model preprocess, which is the foundation of flood simulation and can influence

158   both computational accuracy and efficiency. In this study, a multi-grid generation

159   method was proposed based on the D∞ algorithm, to generate refined grid cells at flood-

160   prone areas where high-resolution representation of topographic features is essential for

161   flood simulation while discretizing the rest of the domain using coarse grids. The D∞

162   algorithm is a method of representing flow directions based on triangular facets in grid

163   DEM proposed by Tarboton (1997). It allocates the flow fractionally to each lower

164   neighboring grid in proportion to the slope toward that grid. The flow direction is

165   determined as the direction of the steepest downward slope on the eight triangular facets

166   formed across a 3×3-pixel window centered on the pixel of interest, which was detailed

167   by Tarboton (1997). Compared with the D8 algorithm, where the flow is discretized

168   into only one of eight possible directions, separated by $45°$, the D∞ algorithm is more

169   reasonable and accurate for delineating the actual river trend.

170   The process of discretizing computational domain based on the D∞ algorithm is

171   shown in Figure 3. First, a raw DEM was prepared, and sink filling was performed on

172   the DEM. Second, the D∞ algorithm was applied to determine the flow direction on

173   grids. Subsequently, the upslope area, defined as the total catchment area that is

174   upstream of a grid center or short length of contour (Moore et al., 1991), was calculated

175   based on the flow direction. Finally, an area threshold was defined to identify the slope

176   lands and derive the river drainage networks from accumulated drainage areas. In a grid

177   cell, if the upslope area was larger than the predefined threshold, it was considered as a

178   river drainage network; otherwise, it was defined as slope lands. The generated slope

179   lands and river network were verified through field surveys or satellite images-based

180   estimates. Generally, the river drainage networks present low slopes and hydraulic

181   conveyance, which is subject to flooding. Areas prone to waterlogging, characterized

182   by persistent water saturation, frequently occur adjacent to rivers. The dynamics of

183   inundation in these low-lying zones constitute a central aspect of our investigation.

184   Therefore, these areas should be discretized using fine grids to represent the flooding

185   process in high resolution. However, in the slope lands, fine grids were not required

186   and coarse grids were used to improve computational efficiency. Because the regions

187   of interest were of high resolution, the reliability of the prediction would not deteriorate,

188   although the number of grid cells was considerably reduced, which can increase model

189   efficiency and capability for flood simulations over large domains. Compared with

190   manual work, the grid generation based on the D∞ algorithm can both reduce workload

191   and time.
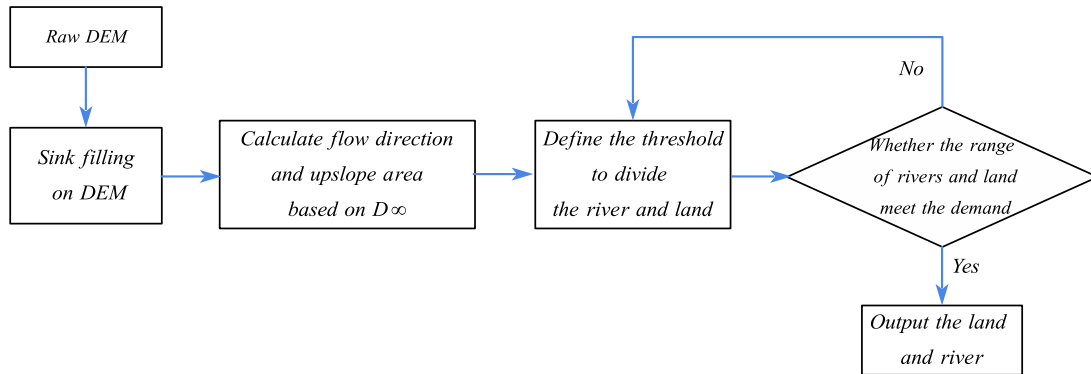
192

193   Figure 3 Grid generation based on the D∞ algorithm

194   AMR dynamically adapts the grid resolution during the simulation, refining the

195   grid locally based on domain characteristics or flow conditions. AMR is commonly

196   employed in scenarios where flow characteristics exhibit abrupt variations, such as

197   aerodynamic shock waves, hydraulic jumps, and tsunami waves. Capturing

198   discontinuous solutions necessitates local grid refinement, with the location of

199   refinement dynamically adapting to the position of the discontinuities. Consequently,

200   AMR are indispensable. However, AMR needs to segment and merge the grid elements

201   repeatedly during the calculation, which can be time-consuming and offset the

202   calculation time saved by the optimized grid. Besides, the mesh generation and flood

203   simulation were compiled in the same code base, which increased the computation cost

204   and time.

205   Flow characteristic variations arising from abrupt geometric changes in the

206   computational domain can be captured using static local refinement grids, provided that

207 the extent of these changes is limited. This approach offers computational time savings.

208 In flood simulations, inundation regions are typically situated in low-lying 2D regions.

209 The outer boundary of the inundation regions can be determined using DEM or

210 calculating by hydrologic models. The D∞ algorithm was employed to preemptively

211 estimate the extent of these areas, providing enhanced computational efficiency relative

212 to AMR and obviating the uncertainty and complexity associated with manual

213 subdivision of the computational domain.

214   A schematic of grid generation is shown in Figure 4. Two types of connecting

215 interfaces are presented, which divide the computing domain into three parts. The first

216 type is the red line (Variable Interpolation Interface, VII) between the coarse and fine

217 grids. The grid cell size changes suddenly on both sides of this line. The second type

218 (Coupling Moving Interface, CMI) is marked in blue on fine grids, which is moving

219 and time-dependent. The first part represents the coarse-grid areas, where the

220 hydrologic model is used to simulate rainfall-runoff. The other two parts are located in

221 the fine-grid areas. The regions between VII and CMI are defined as intermediate

222 transition zones, where the hydrologic model is used to simulate the flooding process.

223 These transition zones facilitate the application of different time steps in different grid

224 cell sizes to improve computational efficiency. The hydrologic and hydrodynamic

225 models are dynamically coupled to represent the flooding process on fine grids, and the

226 CMI is a coupling boundary.
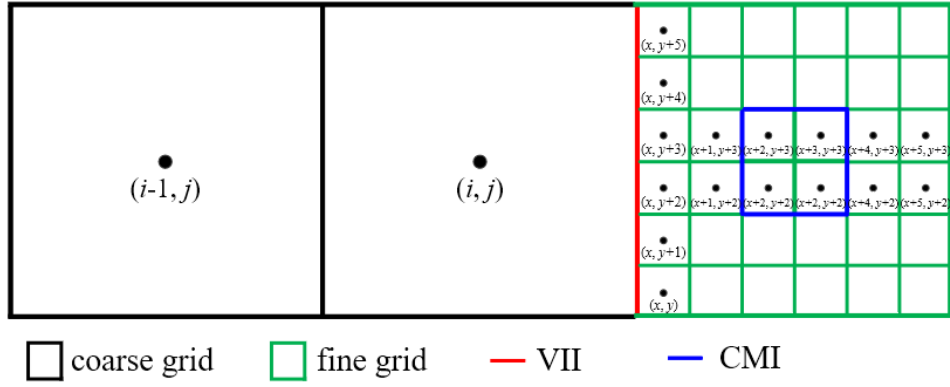
Figure 4. Schematic diagram of grid generation, where i and j are the coordinates of coarse grid; x and y are the coordinates of fine grid; VII is the Variable Interpolation Interface and CMI is the Coupling Moving Interface

2.2 Variable interpolation between coarse and fine grids

During a flow computation, if a cell has a neighbor of different size, interpolation may be required to approximate variables in certain locations so that the governing equation can be solved smoothly. An example is presented in Figure 5(a), where the coarse grid has two eastern neighbors that are half its size. In this case, the variable values of the smaller cells are obtained from those of larger cells. In the traditional method, these variables are directly calculated using certain interpolation methods. There are shared (P_1, P_2) and hanging (Q) nodes at the interface between the coarse and fine grids. In Shen et al. (2021), the variable values on shared nodes can be transmitted directly, while the values on hanging nodes were obtained by linear interpolation of the shared nodes. This method is simple, feasible and easy to use. However, the variable values are stored at the cell center, and there are no values at the interface nodes. Shen et al. (2021) assumed that the values at the interface nodes were equal to that at the cell center. It is inaccurate to make such an assumption, which can bring errors. And the resulting error will increase as the cell size increases.

To overcome these drawbacks, ghost cells and bilinear interpolation method were

247   used to interpolate variables between coarse and fine grids. Figure 5(a) shows the

248   variable interpolation between the coarse and fine grids. Two ghost fine cells were

249   created, which were overlaid with partial coarse grids. The variables on the ghost fine

250   cells were interpolated through the coarse and fine grids between the interface, which

251   were then used as the boundary conditions for the calculation of the fine grids at the

252   next time step. The bilinear interpolation method was applied. The variable

253   interpolation may involve variables at locations c_1, c_2, c_3, $f_{v1}{}'$, $f_{v2}{}'$, f_1 and f_2 . As the

254   variables are stored at the cell center, the variables at c_1, c_2, c_3, f_1 and f_2 are available

255   directly. The values at $f_{v1}{}'$ and $f_{v2}{}'$ are obtained via natural neighbor interpolation, as

256   follows:

257
$$U_{f_{v1}{}'} = U_{c_1} + \frac{U_{c_2} - U_{c_1}}{y_{c_2} - y_{c_1}}(y_{f_{v1}{}'} - y_{c_1}) \tag{1}$$

258
$$U_{f_{v2}{}'} = U_{c_3} + \frac{U_{c_1} - U_{c_3}}{y_{c_1} - y_{c3}}(y_{f_{v2}{}'} - y_{c_3}) \tag{2}$$

259   where $U_{f_{v1}{}'}, U_{f_{v2}{}'}, U_{c_1}, U_{c_2}, U_{c_3}$ are the variables at locations $f_{v1}{}'$, $f_{v2}{}'$, c_1, c_2, c_3 respectively;

260     $y_{f_{v1}{}'}, y_{f_{v2}{}'}, y_{c_1}, y_{c_2}, y_{c_3}$ are the coordinates in y directions at $f_{v1}{}'$, $f_{v2}{}'$, c_1, c_2, c_3 respectively.

261   And then, the variables of ghost fine cells at f_{v1} and f_{v2} can be calculated based

262   on that at $f_{v1}{}'$ and $f_{v2}{}'$, as follows:

263
$$U_{f_{v1}} = U_{f_{v1}{}'} + \frac{U_{f_1} - U_{f_{v1}{}'}}{x_{f_1} - x_{f_{v1}{}'}}(x_{f_{v1}} - x_{f_{v1}{}'}) \tag{3}$$

264
$$U_{f_{v2}} = U_{f_{v2}{}'} + \frac{U_{f_2} - U_{f_{v2}{}'}}{x_{f_2} - x_{f_{v2}{}'}}(x_{f_{v2}} - x_{f_{v2}{}'}) \tag{4}$$

265   where $U_{f_{v1}}, U_{f_{v2}}$ are the variables of ghost fine cells; U_{f1}, U_{f2} are the variables at f_1, f_2,

266   respectively, which were calculated in the last time step; $x_{f_1}, x_{f_2}, x_{f_{v1}}, x_{f_{v2}}, x_{f_{v1}{}'}$ and $x_{f_{v2}{}'}$

267 are the coordinates in x directions at f_1, f_2, f_{v1}, f_{v2}, f_{v1}', f_{v2}' respectively.

268 The values at f_{v1}, f_{v2} were used as the boundary conditions for the calculation of

269 fine grids.

270 The variable interpolation from fine to coarse grids is presented in Figure 5(b),

271 where one ghost coarse cell was established. The variables of ghost coarse cells were

272 determined according to the fine and coarse grids between the interface. The variable

273 interpolation may involve variables at locations c_v', c_1, f_1, f_2. As the variables are stored

274 at the cell center, the variables at c_1, f_1, f_2 are available directly. The values at c_v' are

275 obtained via natural neighbor interpolation, as follows:

$$U_{c_v'} = U_{f_2} + \frac{U_{f_1} - U_{f_2}}{y_{f_1} - y_{f_2}}(y_{c_v'} - y_{f_2}) \qquad (5)$$

277 where $U_{c_v'}$, U_{f_1}, U_{f_2} are the variables at c_v', f_1, f_2 respectively; $y_{c_v'}$, y_{f_1}, y_{f_2} are the

278 coordinates in y direction at c_v', f_1, f_2 respectively.

279 And then, the variables of ghost coarse cells at c_v can be calculated based on that

280 at c_v', c_1, as follows:

$$U_{c_v} = U_{c_v'} + \frac{U_{c_1} - U_{c_v'}}{x_{c_1} - x_{c_v'}}(x_{c_v} - x_{c_v'}) \qquad (6)$$

282 where U_{c_v} are the variables of ghost fine cells; U_{c_1} are the variables at c_1, which were

283 calculated in the last time step; x_{c_1}, $x_{c_v'}$, x_{c_v} are the coordinates in x direction at c_1, c_v', c_v

284 respectively.

285 The values at c_v were used as boundary conditions for the calculation of coarse

286 grids at the next time step.
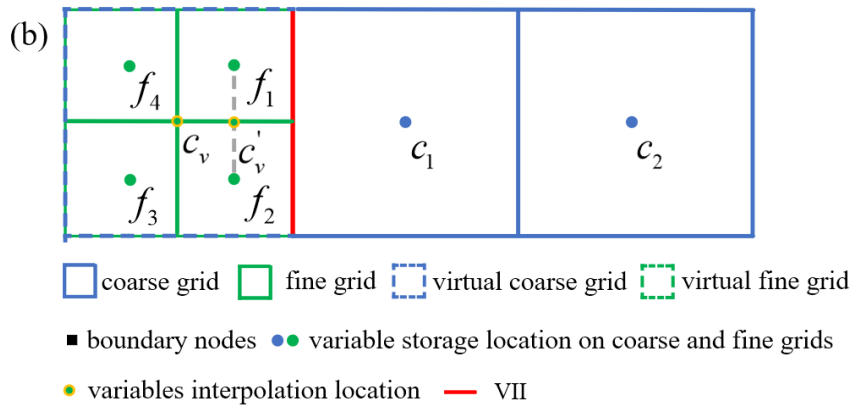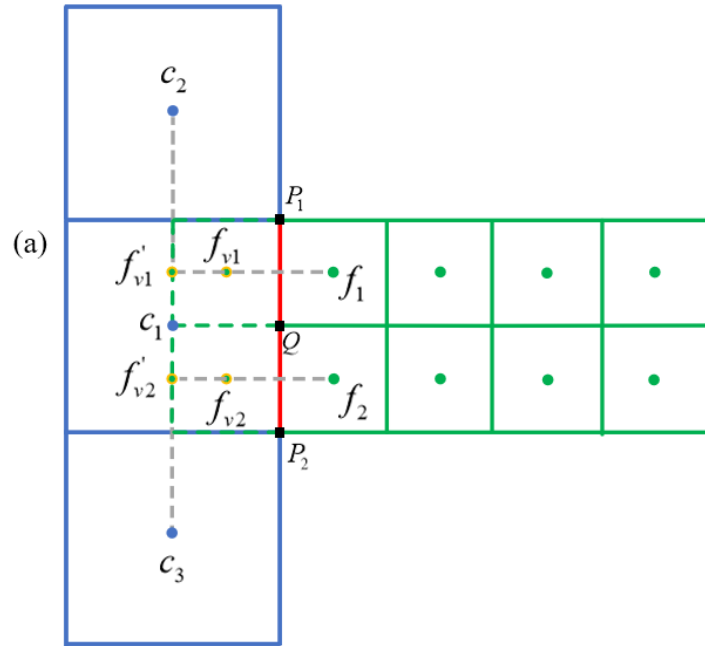
287

288

Figure 5. Variables interpolation between coarse and fine grids: (a) from coarse to

fine grids and (b) from fine to coarse grids

On both sides of the interface between coarse and fine grids, the hydrologic model

was used to simulate the flood process. In the hydrologic model applied to the IM-

DBCM, the Manning equation is employed to simulate surface runoff processes. As a

linear partial differential equation, the Manning equation lacks a nonlinear convection

term. Consequently, the flow state undergoes relatively smooth changes without

exhibiting discontinuous solutions. Linear interpolation is applied to interpolate

variables between coarse and fine grids, with the interpolated values falling within the

range defined by the maximum and minimum values of the interval. This interpolation

299 ensures that the result lies between these bounds, precluding the occurrence of increased

300 flow at the interface of coarse and fine grid transitions.

2.3 Numerical models

2.3.1 Hydrologic model

303 In this study, referring to the runoff calculation in the Storm Water Management

304 Model (SWMM), a 2D NLR model, including water balance and Manning equations,

305 was used to simulate rainfall-runoff. In SWMM, the watershed is divided into many

306 water tanks or reservoirs, where 1D NLR model including water balance and 1D

307 Manning equations is used to simulate the runoff (Rossman, 2015). It is a simple and

308 efficient method to calculate the runoff routing. In reality, however, the runoff routing

309 is a 2D way, so it is not accurate to calculate the 2D runoff routing using 1D NLR model.

310 Also, it is difficult to directly couple the 1D NLR model with 2D hydrodynamic model.

311 Therefore, the 2D NLR model was used to simulate the 2D surface runoff routing in

312 this study, as shown in Eqs. (7-11). The effects of subsurface runoff are assumed to be

313 negligible, which is reasonable for the intense rainfall-induced flood events considered

314 in this study (Hou et al., 2018; Li et al. 2021).

$$\frac{V_i^{n+1} - V_i^n}{\Delta t} = \left(Q_x\right)_{in\ i} - \left(Q_x\right)_{out\ i} + \left(Q_y\right)_{in\ i} - \left(Q_y\right)_{out\ i} + A_i q_{r\ i}^n \tag{7}$$

$$\left(Q_x\right)_{in\ i} - \left(Q_x\right)_{out\ i} = -\sum_{l=1}^{L}\left(q_{x\Gamma}^n \cdot n_x\right)_l \Delta L_l \tag{8}$$

$$\left(Q_y\right)_{in\ i} - \left(Q_y\right)_{out\ i} = -\sum_{l=1}^{L}\left(q_{y\Gamma}^n \cdot n_y\right)_l \Delta L_l \tag{9}$$

$$q_x = \frac{h^{5/3} S_x^{1/2}}{n_r} \tag{10}$$

$$q_y = \frac{h^{5/3} S_y^{1/2}}{n_r} \tag{11}$$

320 where the superscript n and $n+1$ is the time step; V is the water volume of grid (m³);

321 $(Q_x)_{in\,i}$, $(Q_x)_{out\,i}$ is the inflow and outflow of grid i in x direction (m³/s);

322 $(Q_y)_{in\,i}$, $(Q_y)_{out\,i}$ is the inflow and outflow of grid i in y direction (m³/s); $q_{r\,i}$ indicates

323 runoff rate of grid i (mm/h), which is rainfall intensity minus infiltration rate; A_i is the

324 area of grid i (m²); q_x, q_y are the unit discharge stored at cell-center along x and y

325 direction (m²/s), with h, u and v being water depth (m), flow velocity (m/s) in x and y

326 directions, respectively; $q_{x\,\Gamma}, q_{y\,\Gamma}$ are the unit discharge at grid boundary in x and y

327 direction, respectively (m²/s), which are calculated based on q_x, q_y; ΔL_l is the side

328 length of grid (m); $l = 1, 2, 3, \dots, L$ is the number of edges of cell; n_r is the Manning

329 roughness coefficient; S_x and S_y are water level gradients along x and y direction,

330 respectively; $S_x = -\partial(z_b + h)/\partial x$, $S_y = -\partial(z_b + h)/\partial y$,where z_b is the surface

331 elevation.

332 **2.3.2 Hydrodynamic model**

333 The 2D SWEs, consisting of mass and momentum conservation equations (Toro

334 2001), were used to represent the hydrodynamic model.

335
$$\frac{\partial U}{\partial t} + \frac{\partial F}{\partial x} + \frac{\partial G}{\partial y} = S \tag{12}$$

336
$$U = \begin{pmatrix} h \\ hu \\ hv \end{pmatrix},\ F = \begin{pmatrix} hu \\ huu + gh^2/2 \\ huv \end{pmatrix}, G = \begin{pmatrix} hv \\ huv \\ hvv + gh^2/2 \end{pmatrix}, S = \begin{pmatrix} q_r \\ -gh\dfrac{\partial z}{\partial x} - \dfrac{g}{C^2}u\sqrt{u^2 + v^2} \\ -gh\dfrac{\partial z}{\partial y} - \dfrac{g}{C^2}v\sqrt{u^2 + v^2} \end{pmatrix}$$

337 where U is the conserved variables; F, G are the convection term in the x and y

338 directions; S is the source term; C is Chezy's coefficient, $C = \dfrac{1}{n_r}R^{1/6}$,where n_r is the

339   Manning roughness coefficient and R is the hydraulic radius.

340   The Finite Volume Method for Conservative Scheme was used to solve the SWEs,

341   which can ensure local mass and momentum conservation in each control volume cell.

342   The Eq. (12) can be discretized based on structured grids, as follows:

343
$$U_{i,j}^{n+1} = U_{i,j}^{n} - \frac{\Delta t}{A_{i,j}} \sum_{l=1}^{L} \left[F^{l}\left(U_{i,j}^{n}\right) dy - G^{l}(U_{i,j}^{n}) dx \right] + \frac{\Delta t}{A_{i,j}} S\left(U_{i,j}^{n}\right) \tag{13}$$

344   where the superscript n and $n+1$ is the time step; the subscript i, j refers to the grid i, j;

345   dx and dy are the grid edge length. The meaning of other symbols is the same as before.

346   The Harten-Lax-van Leer contact (HLLC) approximate Riemann solver was used

347   to solve the convection term. The second-order accuracy in temporal and spatial

348   discretization was obtained based on the Runge-Kutta method and Monotone

349   Upstream-centered Schemes for Conservation Laws (MUSCL) (Van Leer, 1979). The

350   solution of SWEs was detailed in many references (Toro 2001).

351   **2.4 Dynamic bidirectional coupling of hydrologic and hydrodynamic models**

352   The hydrologic and hydrodynamic models were coupled dynamically and bi-

353   directionally. A water depth threshold was defined in advance and used to determine

354   the state of the cell. In a grid cell, if the water depth was lower than the predefined

355   threshold, it was defined as a non-inundation region where the hydrologic model was

356   applied. Conversely, if the water depth was higher than the threshold, it was considered

357   an inundation region where the 2D hydrodynamic model was applied. When the rainfall

358   intensity increased, the water depth increased because of the gradual accumulation of

359   surface water volume. Once the water depth exceeds the predefined threshold, the non-

360   inundation regions defined last time step may change to the inundation regions. The

361   inflow discharge positions, flow path, and discharge values subsequently changed.

362   Therefore, a CMI was formed between the inundation and non-inundation regions and

363   the hydrologic and 2D hydrodynamic models were coupled bi-directionally through this

364   CMI.

365   The hydrologic model is rational for the continuous non-inundation regions, and

366   the hydrodynamic model is rational for the continuous inundation regions. However,

367   since discontinuity existed at the CMI, the single hydrologic or hydrodynamic models

368   were not acceptable, which was a challenge for the model calculation, as shown in

369   Figure 6. The key issue with the coupled model was to establish a reasonable approach

370   for determining the fluxes passing through the coupling interface, which should

371   integrate the effect of the current flow state obtained from these two models on both

372   sides of the coupling interface.

Non-inundation regions   **CMI**   Inundation regions
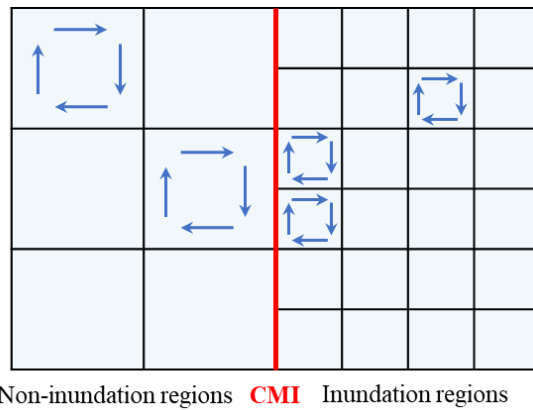
373

374   Figure 6. Model calculation at inundation regions, non-inundation regions and CMI

375   A pair of characteristic waves was used to determine the fluxes calculation

376   methods through the CMI. The characteristic waves were calculated as follows:

$$S_L = u_{i,j} - \sqrt{gh_{i,j}} \tag{1}$$

$$S_R = u_{i+1,j} - \sqrt{gh_{i+1,j}} \tag{2}$$

379   where S_L and S_R are the characteristic waves; u is the flow velocity (m/s); h is the

380   water depth (m); subscript (i, j) and $(i+1, j)$ refer to the cells in non-inundation and

381   inundation regions, respectively.

382   If $S_R > 0$ and $S_L > 0$, the fluxes through the CMI were calculated by the

383   hydrologic model, and the CMI may move toward the non-inundation regions.

384   Therefore, the non-inundation regions shrunk, whereas the inundation regions

385   expanded. Only mass conservation through the CMI can be considered in this situation.

386   If $S_L < 0 < S_R$, the fluxes were calculated by both hydrologic and hydrodynamic

387   models, and the CMI remained unchanged.

388   If $S_L < 0$ and $S_R < 0$, the fluxes are calculated by the hydrodynamic model, and

389   the CMI may move toward inundation regions. Therefore, the inundation regions

390   shrunk, whereas the non-inundation regions expanded. Both the mass and momentum

391   conservation through the coupling boundary were obtained in the latter two situations.

392   The couplings were detailed in Jiang et al. (2021) and Shen et al. (2021).

393   **2.5 Time step**

394   An explicit scheme was used to solve the hydrologic and hydrodynamic models

395   over time. The time step was constrained by the Courant-Friedrichs-Lewy condition

396   (Delis and Nikolos, 2013), where the time step was a dynamic adjustment based on the

397   velocity and water depth in the computational domain. Different time steps were

398   adopted for the coarse and fine grids, and the time step of the fine grids was determined

399   as follows:

400
$$\Delta t_f = C \cdot min\left(\frac{min\left(\Delta x_f\right)}{max\left(\left|u_f\right| + \sqrt{gh_f}\right)}, \frac{min\left(\Delta y_f\right)}{max\left(\left|v_f\right| + \sqrt{gh_f}\right)} \right) \tag{14}$$

401   where Δt_f is the time step of fine grids; C is a constant used to maintain format stability;

402   Δx_f and Δy_f are the side lengths of fine grid in x and y directions; u_f and v_f are the

403   flow velocities on fine grids along x and y directions, respectively; h_f is the water depth

404   on fine grids.

405   The time step of the coarse grids (Δt_c) was determined based on that of the fine

406   grids. If the size of the coarse grid was k times that of the fine grid, the time step of the

407   coarse grid was determined to be $\Delta t_c = k\Delta t_f$.

3 Results

409   The performance of the IM-DBCM was analyzed by applying it to two 2D rainfall-

410   runoff experiments and one real-world flooding process. And the OM-DBCM

411   developed by Shen et al. (2021) was applied to the same cases for comparison with the

412   IM-DBCM.

3.1 Rainfall over a plane with varying slope and roughness

414   In this case, a sloping plan measuring $500m \times 400m$ was designed, with slopes

415     $S_{ox} = 0.02 + 0.0000149x$ and $S_{oy} = 0.05 + 0.0000116y$ along the x and y directions,

416   respectively (Jaber and Mohtar, 2003). The Manning coefficient is equal to

417     $n = \sqrt{n_x^2 + n_y^2}$, where $n_x = 0.1 - 0.0000168x$ and $n_y = 0.1 - 0.0000168y$. The rainfall

418   intensity is given by a symmetric triangular hyetograph $r = r(t)$, with

419     $r(0) = r(200\,\text{min}) = 0$ and $r(100\,\text{min}) = 0.8 \times 10^{-5}\,m/s$. The total simulation time was

420   14,400 s.

421   Different cases with various grid resolutions were developed to divide the

422   computational domain based on the D∞ algorithm, as listed in Table 1. In these cases,

423   the size of all the fine grids was $1m \times 1m$. The grid discretization of different cases is

424   shown in Figure S1 in Supplement.

425   Table 1 Different cases designed to simulate

Cases	The ratio of coarse to fine grids	Number of grids
case12	1:2	112,100
case15	1:5	86,840
case10	1:10	83,220

426   The hydrographs at the outlet node of coordinates of (500m, 400m) obtained from

427   different models are shown in Figure 7. A model proposed by Jaber and Mohtar (2003)

428   was also used to simulate the overland runoff. Because finer grids and small time step

429   were used to divide the computational domain to obtain more accurate results in the

430   model developed by Jaber and Mohtar (2003), the results calculated by Jaber and

431   Mohtar (2003) can be used as a reference solution.

432   From Figure 7, the IM-DBCM held a shape close to the results simulated by Jaber

433   and Mohtar (2003) in all cases, as well as the peak discharge. But the peak discharge

434   of the hydrograph is slightly overestimated by the OM-DBCM, which may be attributed

435   to the difference in the variable interpolation between the coarse and fine grids. In the

436   OM-DBCM, variables at the interpolation interface were equal to that at the cell center,

437   which was then used to interpolate variables between the coarse and fine grids through

438   shared and hanging nodes. This interpolation method had two drawbacks. Firstly, it is

439   not reasonable to assume the variables at the interpolation interface are equal to that at

440   the cell center, and the resulting error could increase as the grid size increases. Besides,

441   compared with bilinear interpolation, the values at the hanging nodes are calculated by

442   linear interpolation through shared nodes, which may result in relatively large errors.

443   The results show that the methods to interpolate variable between the coarse and fine

444   grids by developing ghost cells proposed in this study has acceptable accuracy.

445   To quantitatively assess the performance of IM-DBCM, the Root Mean Square

446   Error (RMSE) of different cases was computed. The RMSEs of case12, case15 and

447   case10 were 4.01E-04, 7.85E-03 and 3.25E-02, respectively. It is showed that the error

448   gradually increased with the increasing of the ratio of coarse to fine grids. The IM-

449   DBCM may capture the shape of the hydrograph in case12 and case15, both in limbs

450   and peak discharge, but the peak discharge is slightly underestimated in case10. A

possible explanation is that, compared to the coarse grids, the fine grids could better

capture the geometry of the channel cross-sections. High-resolution grids can better

represent small-scale topographic features and flow passages (Hou et al., 2018);

consequently, the simulation results on case12 and case15 are more satisfactory than

those on case10. Similarly, the simulation accuracy of the OM-DBCM also gradually

decreased with the increasing of the ratio of coarse to fine grids. Overall, the benefit of

using the IM-DBCM for the flood simulations is evident.
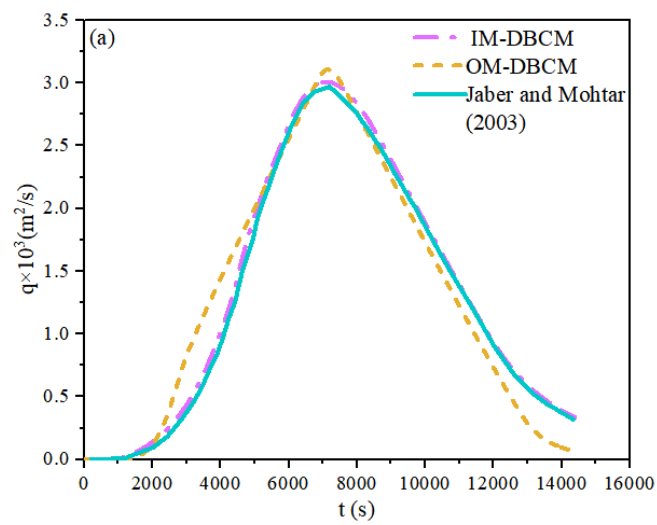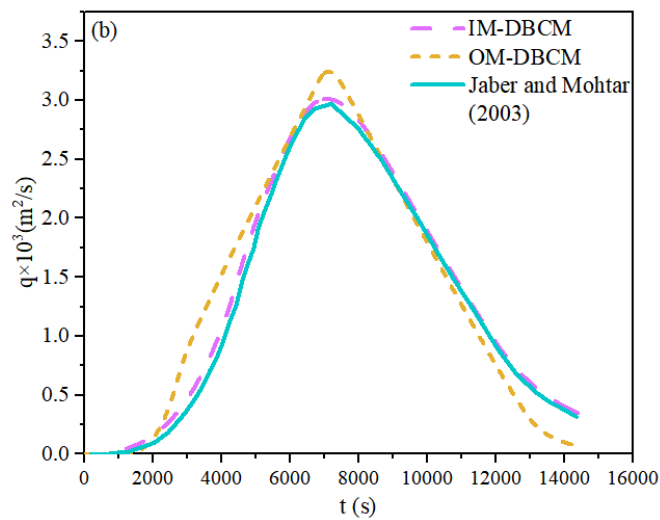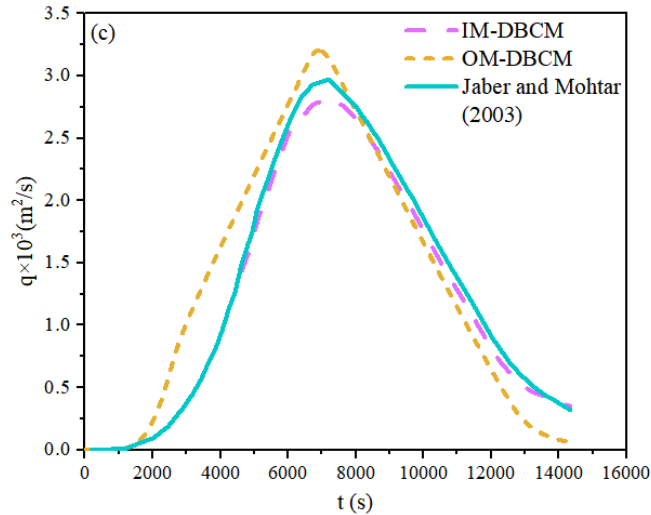
460

461   Figure 7. Hydrographs obtained from different models: (a) case12, (b) case15 and (c)

462   case10

3.2 V-shaped catchment

464   A 2D surface flow simulation was conducted over a V-shaped catchment to

465   evaluate the performance of the IM-DBCM. The computational domain is

466   symmetrically V-shaped, with two symmetrical hillslopes converging to form a channel

467   in the central region. The river bed slopes -0.05 on the left side and 0.05 on the right

468   side. The channel bed has zero slope in the x direction and a slope of 0.02 in the y

469   direction. The Manning coefficient is 0.015 on the hillslope and 0.15 on the main

470   channel. The detailed dimensions and associated information pertaining to the V-

471   shaped catchment are presented in Figure 8. The total simulation time was 10,800 s,

472   with a constant rainfall intensity of 10.8 mm/h applied for 5,400 s.

473
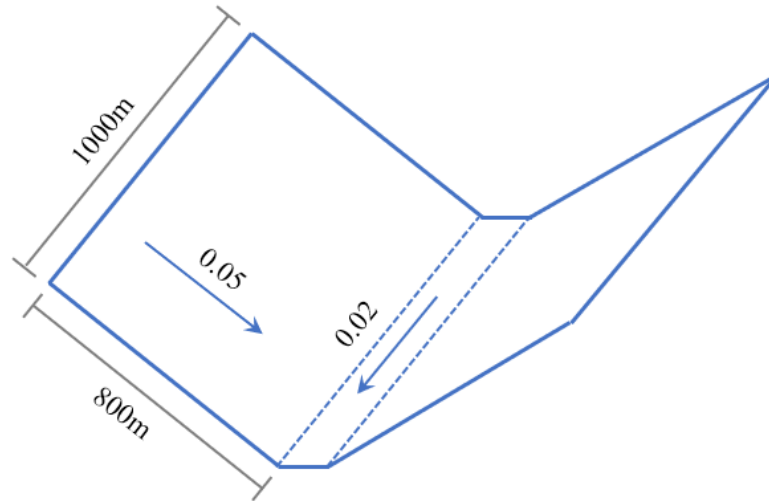
474   Figure 8. Geometry and size of the V-shaped catchment

475   The IM-DBCM was used to simulate the 2D surface flow over the V-shaped

476   domain. The computational basin was divided into coarse and fine grids based on the

477   D∞ algorithm. The size of the fine grids was 10m × 10m, whereas that of the coarse

478   grids was 20m × 20m. The grid partition is presented in Figure S2 in Supplement, where

479   a V-shaped zones near the watershed outlet was discretized using fine grids, while the

480   remaining areas were discretized using coarse grids.

481   Besides, the HM2D and the coupled Mike SHE and Mike 11 was also developed

482   to simulate the surface flow under the same conditions. In the HM2D, the grid size was

483   set as 10m × 10m. In the coupled Mike SHE and Mike 11, the Mike SHE was used to

484   simulate the rainfall-runoff on the hillslopes and the grid sizes was also 10m × 10m,

485   while the Mike 11 was used to simulate the runoff in the channel. Results were all

486   compared with measured data.

487   The discharge hydrographs obtained from different models are shown in Figure 9.

488   This figure showed a close match between the measured data and the computed results

489   obtained using the IM-DBCM. This indicated that the results were encouraging and the

490   overall trend was well captured. The hydrographs obtained from the IM-DBCM was

491   closer to the analytical solution compared with the coupled Mike SHE and Mike 11.

492   The weir flow equation was utilized to couple the Mike SHE and Mike 11. Notably,

493   only mass was transferred between the models, excluding momentum. However, mass

494   and momentum were exchanged between the hillslopes and river channels. The IM-

495   DBCM model ensured the conservation of both mass and momentum, resulting in

496   simulated hydrographs that closely match analytical solutions.

497   Comparing the hydrographs generated by the 2D hydrodynamic model and IM-

498   DBCM, the discharge hydrographs exhibited congruence for the discharge receding

499   limb and peak discharge. However, the consistency of the hydrographs simulated by

500   these two models was less pronounced for the rising limb. In the rising limb, the flow

501   calculated using IM-DBCM was lower than that simulated using HM2D. The disparity

502   in hydraulic behavior between the hydrodynamic and hydrologic models explains the

503   observed phenomenon. The HM2D consistently simulate the surface flow using the 2D

504   hydrodynamic model; conversely, the hydrologic model was employed solely to

505   simulate the flood processes when the upstream water level recedes below the threshold

506   established in IM-DBCM. In the hydrologic models that lack time-partial derivative

507   terms, the current velocity was solely determined by the instantaneous water level

508   gradient. This differs from the previous calculation method, which added the flux term

509   to the velocity at the previous time step. Consequently, the velocity calculation in 2D

510   hydrodynamic models deviated from the IM-DBCM.
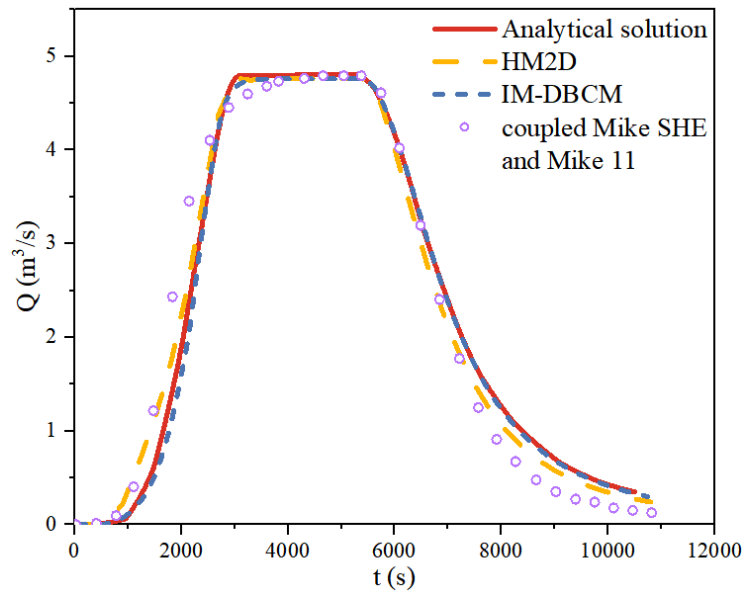
Figure 9. Measured and simulated results obtained from different models

3.3 Flood simulation in a natural watershed

The Goodwin Creek watershed, located in Panola County, Mississippi, USA, is often selected as a benchmark to assess the capability of flood models because of sufficient available observed data. Drainage is westerly to Long Creek which flows into the Yocona River, one of the main rivers of the Yazoo River, a tributary of the Mississippi River. The Goodwin Creek watershed covers an area of 21.3 km^2. The overall terrain gradually decreased from northeast to southwest, which is consistent with the trend of the main channel, and the elevation ranged from 71 to 128 m. The computational basin and bed elevations are shown in Figure 10.

Land use in this watershed was divided into four classes including forest, water, cultivated, and pasture, and their Manning coefficients were 0.05, 0.01, 0.03, and 0.04, respectively (Sánchez, 2002). The infiltration coefficients of different soil types were determined according to Blackmarr (1995). The rainfall event in sixteen rain gages (see Figure 10) of October 17, 1981 was chosen for simulation (Sánchez, 2002), and the inverse distance interpolation method (Barbulescu, 2016) was used to calculate the precipitation over the entire watershed. The rainfall duration was 4.8 h. Rainfall was

529 spatially distributed at different times, as shown in Figure S3 in Supplement. There

530 were measured data in six observation stations (i.e., 1, 4, 6, 7, 8 and 14) (Blackmarr,

531 1995), whose locations were shown in Table S1 in Supplement, and the simulated

532 results were compared with the measured data in these stations.
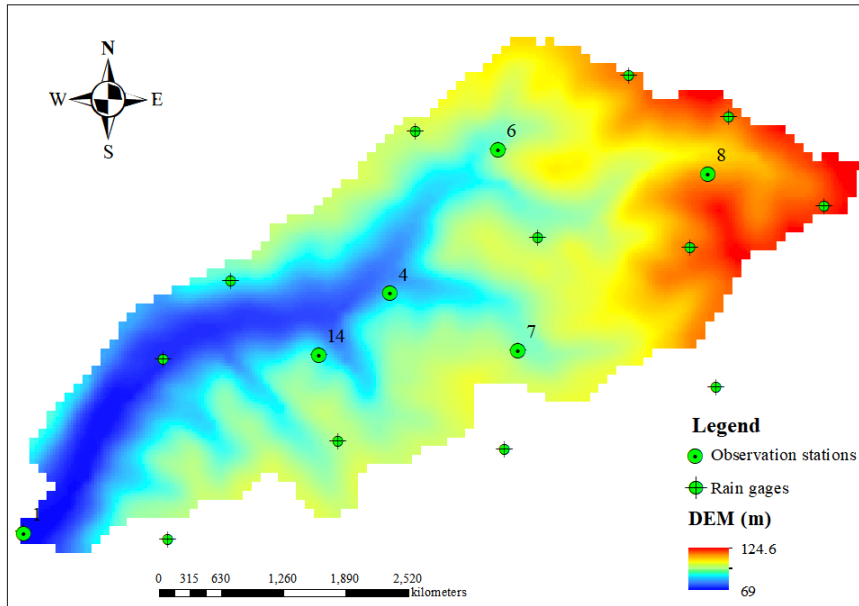
533

534 Figure 10. Overview of the Goodwin Creek watershed

535 The simulations were performed for 12 h. Different cases with various grid

536 resolutions were developed to verify the computational efficiency and numerical

537 accuracy of IM-DBCM, as listed in Table 2. In M-DBCM, the rivers were covered by

538 fine-grid cells with dimensions of 10 m × 10 m, whereas the coarseness in the rest of

539 the domain was increased to higher levels, as presented in Figure S4 in Supplement.

540 Table 2. Different cases designed to simulate the Goodwin Creek watershed

Cases	The ratio of coarse to fine grids	Number of grids
case12	1:2	104,555
case15	1:5	65,240
case10	1:10	59,431

541 The OM-DBCM was also used to simulate the rainfall runoff with the same

542 resolutions. The Nash-Sutcliffe efficiency (NSE) was used to quantify errors in each

543   model. The NSEs of IM-DBCM and OM-DBCM are shown in Table 3. From this table,

544   the NSEs of IM-DBCM were higher than that of OM-DBCM at most stations, which

545   was probably caused by the different interpolation method at the interface between

546   coarse and fine grids. It is verified that the IM-DBCM has relatively high accuracy in

547   simulating rainfall-runoff. In OM-DBCM, it is unreasonable to make the variables at

548   the interface between coarse and fine grids equal to that at the cell center, which can

549   bring errors. The induced error will increase as the ratio of coarse and fine grids increase.

550   Therefore, it is also observed that the NSEs of OM-DBCM decreased with the increased

551   ratio of coarse and fine grids. It is indicated that the ghost cells and bilinear interpolation

552   used in the IM-DBCM to interpolate variables between coarse and fine grids can make

553   the simulation more reasonable.

554   Table 3 NSEs of different models ("IM" and "OM" refer to IM-DBCM and OM-

555   DBCM, respectively)

Station	G1		G4		G6		G7		G8		G14	
Model	IM	OM	IM	OM	IM	OM	IM	OM	IM	OM	IM	OM
case12	0.9496	0.9108	0.9611	0.9011	0.9904	0.8982	0.9658	0.9004	0.9435	0.9104	0.9311	0.8804
case15	0.9399	0.8766	0.9404	0.8800	0.9426	0.8819	0.9258	0.8931	0.9341	0.8942	0.9001	0.7942
case10	0.9207	0.8261	0.8907	0.8435	0.9513	0.7977	0.9358	0.8525	0.9358	0.8678	0.9135	0.8078

556   Figure 11 shows a comparison of the measured and simulated hydrographs by IM-

557   DBCM at the monitoring gauges, whose locations are presented in Figure 10. At all

558   gauges, the hydrographs obtained from different cases were well aligned with the

559   measured data, which indicates that the IM-DBCM could reliably reproduce the flood

560   wave propagation in the complex topography. The results of case12, in general, were

561 better than those of case15 and case10, especially at station G1. A possible explanation

562 is that a finer grid is needed to better capture the watershed geometry and obtain more

563 satisfactory simulation accuracy. The cell size of case15 and case10 is larger than that

564 of case12.

565   Compared with other stations, at station G1, the simulation results obtained from

566 case15 and case10 deviated substantially from the measured data, especially at receding

567 limb of the hydrographs. We deduced that the reason for this discrepancy is not the

568 mesh partitioning, but the location of the G1. G1 is located at the watershed outlet,

569 where water flows out of the watershed from here. The errors generated upstream may

570 be accumulated at this station. Despite the deviation, the overall trend of the

571 hydrographs indicated that the IM-DBCM is satisfactory and can reliably reproduce

572 flood wave propagation in complex topography.
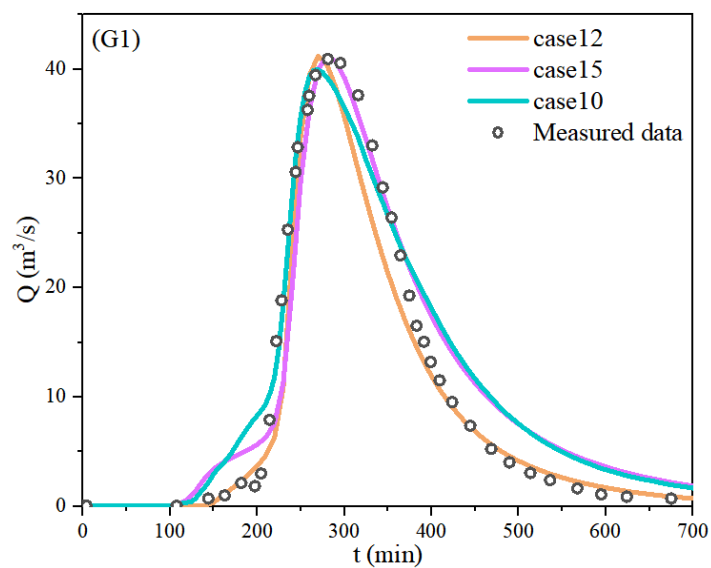
573
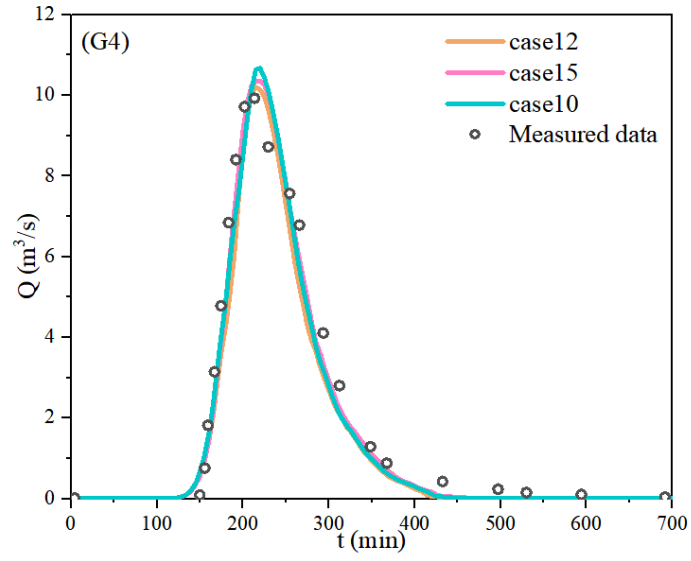
574
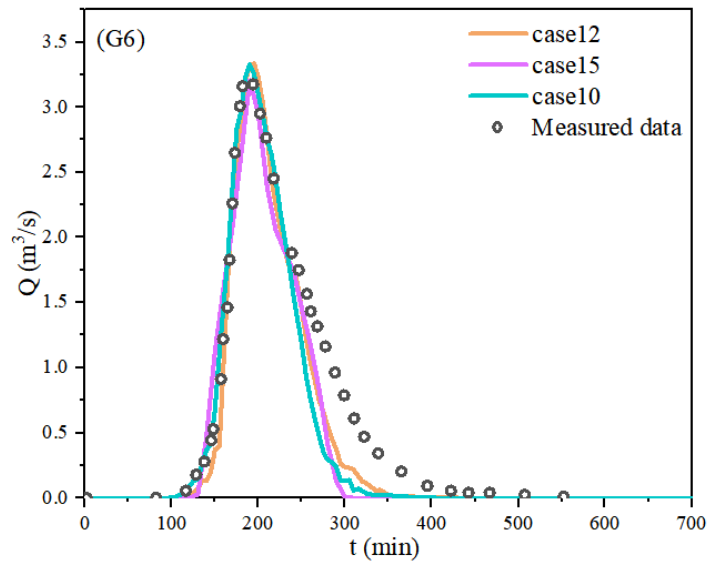
575
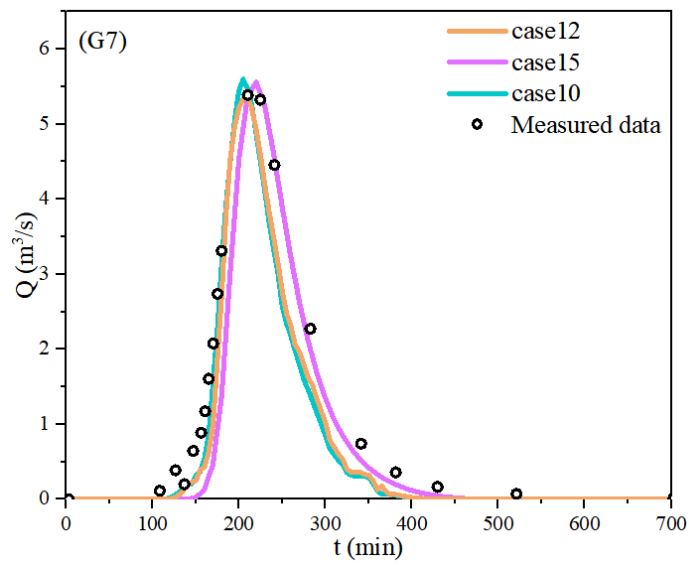
576
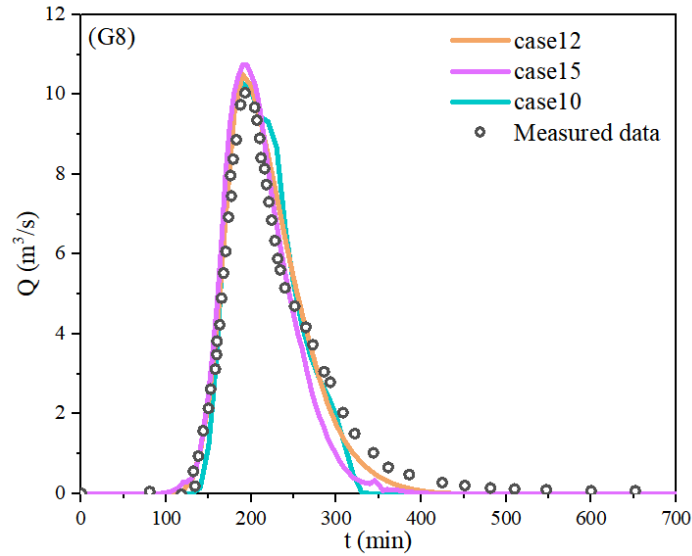
577
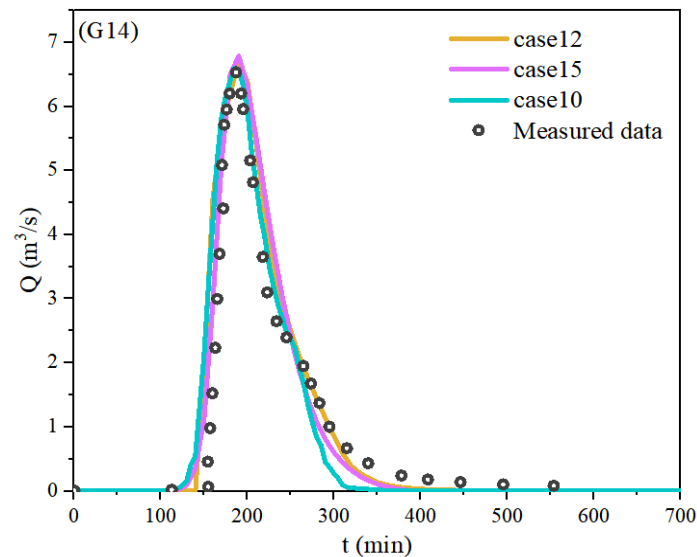
578

579 Figure 11. Hydrographs obtained from different cases

580   The water depth distribution at different times is shown in Figure 12. The

581 probability of flooding and inundation increases with increasing water depth. From 0

582 to 100 min, the water depth in the computational domain increased with the rainfall.

583 The water depth across the computational domain is predominantly shallow, as shown

584 in Figure 12(a). The discharge hydrographs within the watershed reached their peak at

585 200 minutes. Concurrently, the water depth in the watershed attained its maximum level,

586 as shown in Figure 12(b). After 200 min, when rainfall stopped, the water depth in the

587 computational watershed decreased (Figure 12(c)).
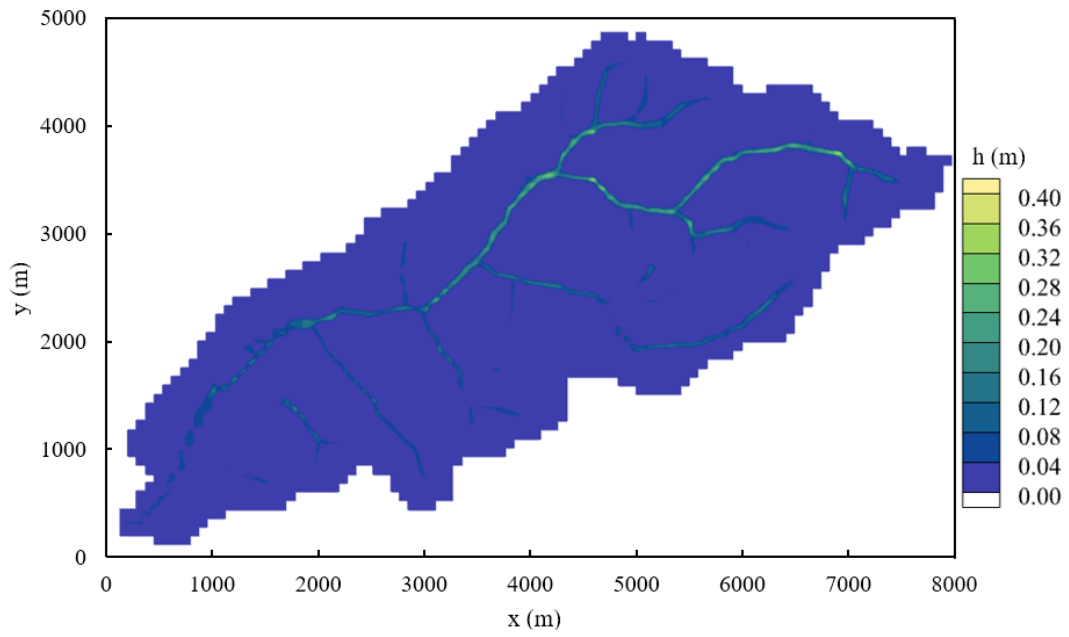
588
589
(a) $t = 100$ min
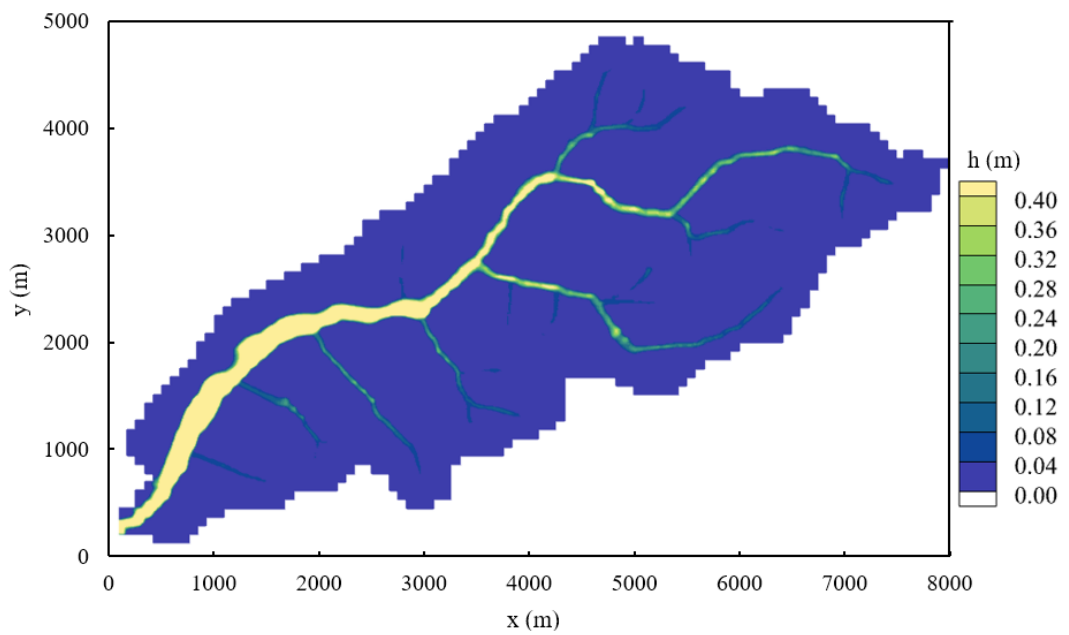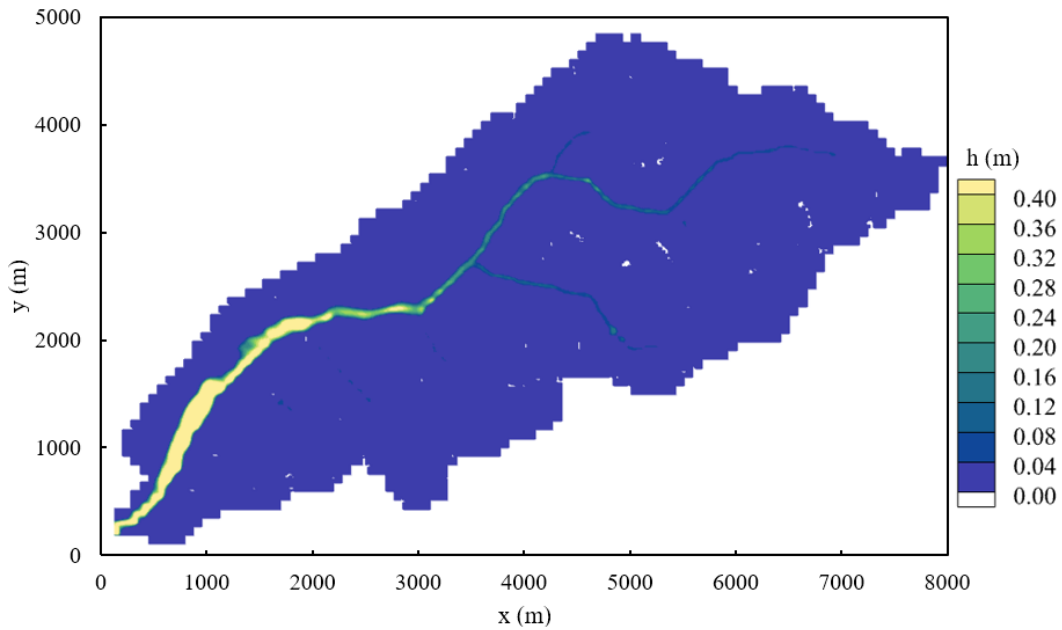
590
591
(b) $t = 200$ min

Figure 12. Water depth at different times

In terms of efficiency, the total execution time of IM-DBCM was compared with the uniform grid-based model (HM2D), as shown in Figure 13. The total execution time of the different cases ranked from highest to lowest is as follows: HM2D> case12> case15> case10. Compared to HM2D, the multi-grid discrete computing domain improves computational efficiency by 60%. Uniform fine grids were used to divide the computing zones in HM2D, and 207,198 computational grids were generated. Compared with HM2D, most of the areas were discretized with coarse grids, and only a small part of the regions was calculated based on fine grids in IM-DBCM; the computational grids of the multi-grid-based model (Table 2) were considerably lower than that of HM2D. Furthermore, case12 required more computational time than case15 and case10. Fewer computational grid nodes were presented in case15 and case10, which required less time for calculation, and the computational efficiency could be further improved. The advantages of using IM-DBCM based on multi-grids for flood simulations are evident. The difference in total runtime between the IM-DBCM and OM-DBCM is the time spent on mesh generation. In the OM-DBCM, the

610 computational domain is divided manually, which is highly subjective, and the

611 computational time varied from person to person.

612   However, there was not a significant difference in the computation time among

613 case12, 15 and 10. The calculation time for coarse grids is shown in Figure 13(b). It is

614 observed that the runtime for coarse grids decreases rapidly in different cases. In case12,

615 case15 and case10, the number of coarse grids is 42517, 7425, and 2153, respectively.

616 As the number of coarse grids decreased significantly, the runtime for these grids also

617 decreased rapidly. The number of fine grids is consistent in case12, case15, and case10,

618 with a calculation time of 4800s. The fine grids number is much greater than that of the

619 coarse grids, especially in case15 and case10. The 2D hydrodynamic model was solved

620 in the fine-grid regions, which cost more computation time compared with the coarse

621 grids where the hydrologic model was applied. The calculation time for fine grids is

622 significantly longer than that for coarse grids, comprising a substantial portion of the

623 overall execution time.

624   In many watersheds, the 2D inundation regions account for a minor proportion of

625 the total watershed area. The fine grids were employed to partition the small inundation

626 regions, while the coarse grids were utilized to discretize the majority of the non-

627 inundation regions. The computational efficiency can be significantly enhanced due to

628 the smaller proportion of fine grids and larger proportion of coarse grids. In the IM-

629 DBCM, the 1D rivers and 2D inundation regions were not distinguished, resulting in

630 their division using fine grids. Consequently, the 2D hydrodynamic model was applied

631 to both regions, leading to an increased computational time. In future studies, the 1D

632 hydrodynamic model will be used to compute the flood evolution specifically in the 1D

633 rivers, leading to a reduction in computational time. Hence, the computational

634 efficiency advantages of the proposed IM-DBCM are more pronounced.
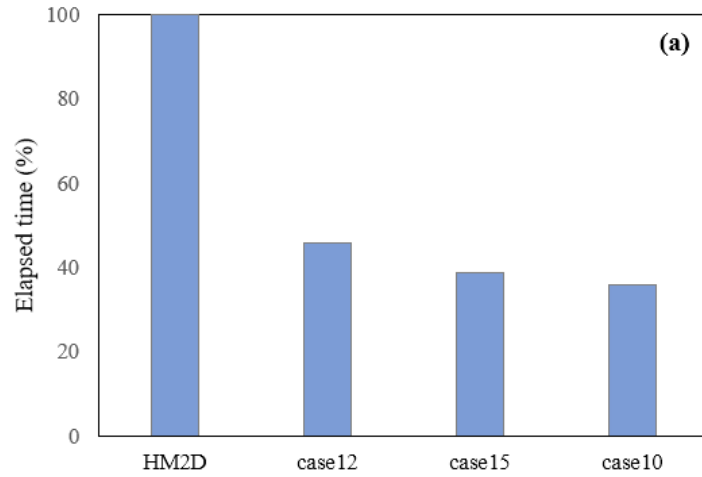
635
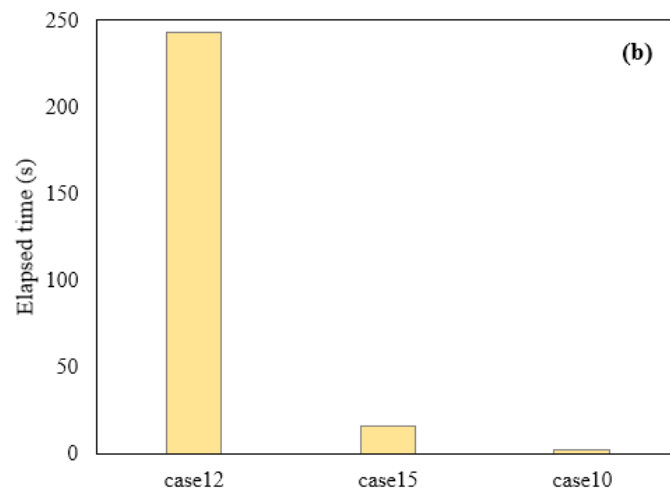
636

637   Figure 13. Computation time of different cases: (a) the relative difference of HM2D

638   and IM-DBCM; (b) the runtime for coarse grids

4 Conclusions

640   An improved dynamic bidirectional coupled hydrologic-hydrodynamic model

641   based on multi-grid (IM-DBCM) was presented in this study. A multi-grid system was

642   generated based on the D∞ algorithm, dividing regions that required high-resolution

643   representation using fine grids and the rest using coarse grids to reduce computational

644   load. A two-dimensional non-linear reservoir was adopted in the hydrologic model,

645   while two-dimensional shallow water equations were applied in the hydrodynamic

646   model. The hydrologic model was applied to the coarse-grid regions, whereas the

647   hydrologic and hydrodynamic models were coupled in a bidirectional manner for the

648   fine-grid areas. Different time steps were adopted in coarse and fine grids. Ghost cells

649   and bilinear interpolation were used to interpolate variables between coarse and fine

650   grids. The hydrologic and hydrodynamic models were dynamically and bidirectionally

651   coupled with a time-dependent and moving coupling interface.

652   The performance of IM-DBCM was verified using three cases. The IM-DBCM

653   was demonstrated to effectively simulate flow processes and ensure reliable simulation.

654   Compared with the OM-DBCM, the results obtained from the IM-DBCM were well

655   aligned with the measured data, and it could reliably reproduce the flood wave

656   propagation in complex topography. In addition to producing numerical results with

657   similar accuracy, the IM-DBCM saved computational time compared with the model

658   on fine grids. Furthermore, a moving coupling interface between the hydrologic and

659   hydrodynamic models was observed in the IM-DBCM. The IM-DBCM has both high

660   computational efficiency and numerical accuracy, which was adapted adequately to the

661   real-life flooding process and provided practical and reliable solutions for rapid flood

662   prediction and management, especially in large watersheds.

663   The IM-DBCM accurately and efficiently reproduces the flooding process and has

664   the potential for a wide range of practical applications. The hydrologic model considers

665   only surface runoff, which is appropriate for the intense rainfall-induced flood events

666   examined in this study. However, a complete hydrologic model should include surface

667   flow, interflow, and underground runoff. In future works, the interflow and

668   underground runoff could be calculated in the hydrologic model.

669   **Data availability**

670   Model simulation and calibration data are available upon request from the

671   corresponding author. Digital elevation model data are provided by the Geospatial Data

672   Cloud at http://www.gscloud.cn. The data sets of Soil Properties and Land cover are

provided by Sánchez (2002) and Blackmarr (1995). The rainfall and measured data were Blackmarr (1995).

Author contributions

Yanxia Shen designed the methodology and carried out the investigation. Qi Zhou provided the original model input data. The study was supervised by Chunbo Jiang. Yanxia Shen prepared the first draft of the manuscript and Zhenduo Zhu revised and improved the original manuscript.

Competing interests

The authors declare that they have no conflict of interest.

Acknowledgements

This study was supported by the National Natural Science Foundation of China (Grant No. 52179068) and the Key Laboratory of Hydroscience and Engineering (Grant No. 2021-KY-04). The authors thank the anonymous reviewers for their valuable comments.

References

Barbulescu, A.: A new method for estimation the regional precipitation. Water Resources Management, 30(1), 33-42, 2016. https://doi.org/10.1007/s11269-015-1152-2

Bates, P.D.: Flood inundation prediction. Annual Review of Fluid Mechanics, 54:287-315, 2022. https://doi.org/10.1146/annurev-fluid-030121-113138

Bhola, P.K., Leandro, J., Disse, M.: Framework for offline flood inundation forecasts for two-dimensional hydrodynamic models. Geosciences (Switzerland), 8(9), 346, 2018. https://doi.org/10.3390/geosciences8090346

Blackmarr, W.: Documentation of hydrologic, geomorphic, and sediment transport measurements on the Goodwin Creek experimental watershed, northern

Mississippi, for the period 1982-1993. Technical Report for United States Department of Agriculture: Oxford, MS, USA, October, 1995.

Bomers, A., Schielen, R.M.J., Hulscher, S.J.M.H.: The influence of grid shape and grid size on hydraulic river modelling performance. Environmental Fluid Mechanics. 19(5), 1273-1294, 2019. https://doi.org/10.1007/s10652-019-09670-4

Cea, L, Puertas, J., Pena, L., Garrido, M.: Hydrologic forecasting of fast flood events in small catchments with a 2D-SWE model, Numerical model and experiment validation. World Water Congress, 1-4, Montpellier, France, 2008.

Caviedes-Voullième, D., García-Navarro, P., Murillo, J.: Influence of mesh structure on 2D full shallow water equations and SCS curve number simulation of rainfall/runoff events. Journal of Hydrology, 448-449(2), 39-59, 2012. https://doi.org/10.1016/j.jhydrol.2012.04.006

Choi, C.C., Mantilla, R.: Development and Analysis of GIS Tools for the Automatic Implementation of 1D Hydraulic Models Coupled with Distributed Hydrological Models. Journal of Hydrologic Engineering, 20, 06015005, 2015. https://doi.org/10.1061/(ASCE)HE.1943-5584.0001202

Costabile, P., Costanzo, C.: A 2D-SWEs framework for efficient catchment-scale simulations: hydrodynamic scaling properties of river networks and implications for non-uniform grids generation. Journal of Hydrology, 599(6402), 126306, 2021. https://doi.org/10.1016/j.jhydrol.2021.126306

Chen, W., Huang, G., Han, Z.: Urban stormwater inundation simulation based on SWMM and diffusive overland-flow model. Water Science and Technology 76(12):3392-3403, 2017. https://doi.org/10. 2166/wst.2017.504

Chen, W., Huang, G., Han, Z., Wang, W.: Urban inundation response to rainstorm patterns with a coupled hydrodynamic model: a case study in Haidian Island,

723   China.   Journal   of   Hydrology   564:1022–1035,   2018.

724   https://doi.org/10.1016/j.jhydrol.2018.07.069

725 Delis, A., Nikolos, I.: A novel multidimensional solution reconstruction and edge-based

726   limiting procedure for unstructured cell-centered finite volumes with application

727   to shallow water dynamics. International Journal for Numerical Methods in Fluids,

728   71: 584-633, 2013. https://doi.org/10.1002/fld.3674

729 Donat, R., Marti M.C., Martinez-Gavara, A., Mulet P.: Well-balanced adaptive mesh

730   refinement for shallow water flows. Journal of Computational Physics, 257:937-

731   53, 2014. https://doi.org/10.1016/j.jcp.2013.09.032

732 Ding, Z.L., Zhu, J.R., Chen, B.R., Bao, D.Y.: A Two-Way Nesting Unstructured

733   Quadrilateral Grid, Finite-Differencing, Estuarine and Coastal Ocean Model with

734   High-Order Interpolation Schemes. Journal of Marine Science and Engineering,

735   9(3), 335, 2021. https://doi.org/10.3390/jmse9030335

736 Feistl, T., Bebi, P., Dreier, L., Hanewinkel, M., Bartelt, P.: A coupling of hydrologic

737   and hydraulic models appropriate for the fast floods of the Gardon river basin

738   (France). Natural Hazards & Earth System Sciences, 14(11), 2899-2920, 2014.

739   https://doi.org/10.5194/nhess-14-2899-2014

740 Garcia-Navarro P., Murillo J., Fernandez-Pato J., Echeverribar I., Morales-Hernandez

741   M.: The shallow water equations and their application to realistic cases.

742   Environmental   fluid   mechanics.   19(5):   1235-1252,   2019.

743   https://doi.org/10.1007/s10652-018-09657-7

744 Ghazizadeh, M.A., Mohammadian, A., Kurganov, A.: An adaptive well-balanced

745   positivity preserving central-upwind scheme on quadtree grids for shallow water

746   equations.   Computers   &   Fluids.   208,   104633,   2020,

747   https://doi.org/10.1016/j.compfluid.2020.104633

748 Hu, R., Fang, F., Salinas, P., Pain, C.C.: Unstructured mesh adaptivity for urban

749   flooding modelling. Journal of Hydrology 560,354-363, 2018.

750   https://doi.org/10.1016/j.jhydrol.2018.02.078

751 Hou, J., Wang, R., Liang, Q., Li, Z., Huang, M.S., Hinkelmann, R.: Efficient surface

752   water flow simulation on static cartesian grid with local refinement according to

753   key topographic features. Computers & Fluids, 176, 117-134, 2018.

754   https://doi.org/10.1016/j.compfluid.2018.03.024

755 Hou J., Liu F., Tong Y., Guo K., Li D.: Numerical simulation for runoff regulation in

756   rain garden using 2D hydrodynamic model. Ecological Engineering, 153(2),

757   105794, 2020. https://doi.org/10.1016/j.ecoleng.2020.105794

758 Jaber, F.H., Mohtar, R.H.: Stability and accuracy of two-dimensional kinematic wave

759   overland flow modeling. Advances in Water Resources, 26(11): 1189-1198, 2003.

760   https://doi.org/10.1016/S0309-1708(03)00102-7

761 Jiang, C., Zhou, Q., Yu, W., Yang, C., Lin, B.: A dynamic bidirectional coupled surface

762   flow model for flood inundation simulation. Natural Hazards and Earth System

763   Sciences, 21(2), 497-515, 2021. https://doi.org/10.5194/nhes-21-497-2021

764 Kim, J., Warnock, A., Ivanov, V.Y., Katopodes, N.D.: Coupled Modeling of

765   Hydrologic and Hydrodynamic Processes Including Overland and Channel Flow.

766   Advances in Water Resources, 37, 104-126, 2012.

767   https://doi.org/10.1016/j.advwatres.2011.11.009

768 Kesserwani, G., Sharifian, M.K.: (Multi)wavelet-based Godunov-type simulators of

769   flood inundation: Static versus dynamic adaptivity. Advances in water resources,

770   171,104357, 2023. https://doi.org/10.1016/j.advwatres.2022.104357

771 Li, Z., Chen, M.Y., Gao, S., Luo, X.Y., Gourley, J.J., Kirstetter, P., Yang, T.T., Kolar,

772   R., McGovern, A., Wen, Y.X., Rao, B., Yami, T., Hong, Y. (2021). CREST-IMAP

v1.0: a fully coupled hydrologic-hydraulic modeling framework dedicated to flood inundation mapping and prediction. Environmental Modelling and Software, 141(1), 105051. http://doi.org/10.1016/j.envsoft.2021.105051

Moore, I.D., Grayson, R.B., Ladson, A.R.: Digital terrain modelling: a review of hydrological, geomorphological, and biological applications. Hydrological Processes, 5(1), 3-30, 1991. https://doi.org/10.1002/hyp.3360050103

Ozgen-Xian, I., Kesserwani, G., Caviedes-Voullieme, D., Molins, S., Xu, Z.X., Dwivedi, D., Moulton, J.D., Steefel, C.I.: Wavelet-based local mesh refinement for rainfall-runoff simulations. Journal of Hydroinformatics, 22(5), 1059-1077, 2020. https://doi.org/10.2166/hydro.2020.198

Rossman, L.A. Storm Water Management Model User's Manual Version 5.1; EPA/600/R-14/413b; U.S. Environmental Protection Agency: Cincinnati, OH, USA, 2015.

Schumann, G.J.P., Neal, J.C., Voisin, N., Andreadis, K.M., Pappenberger, F., Phanthuwongpakdee, N., Hall, A.C., Bates, P.D.: A first large-scale flood inundation forecasting model. Water Resource Research 49(10):6248–6257, 2013. https://doi.org/10.1002/wrcr.20521

Sánchez, R.R.: GIS-Based Upland Erosion Modeling, Geovisualization and Grid Size Effects on Erosion Simulations with CASC2D-SED. Ph.D. Thesis, Colorado State University, Fort Collins, CO, USA, 2002.

Singh J., Altinakar M.S., Yan D.: Two-dimensional numerical modeling of dam-break flows over natural terrain using a central explicit scheme. Advances in Water Resources, 34(10), 1366-1375, 2011. https://doi.org/10.1016/j.advwatres.2011.07.007

Seyoum. S.D., Vojinovic, Z., Price, R.K., Weesakul, S.: Coupled 1D and noninertia 2D

flood inundation model for simulation of urban flooding. Journal of Hydraulic Engineering 138(1):23–34, 2012. https://doi.org/10.1061/(ASCE)HY.1943-7900.0000485

Shen, Y., Jiang, C., Zhou, Q., Zhu, D., Zhang, D.: A Multigrid Dynamic Bidirectional Coupled Surface Flow Routing Model for Flood Simulation. Water, 13, 3454, 2021. https://doi.org/10.3390/w13233454

Shen, Y., Jiang, C.: Quantitative assessment of computational efficiency of numerical models for surface flow simulation. Journal of Hydroinformatics, 25 (3): 782–796, 2023. https://doi.org/10.2166/hydro.2023.131

Tarboton, D.G.: A new method for the determination of flow directions and upslope areas in grid digital elevation models. Water Resources Research, 33(2), 662-670, 1997. https://doi.org/10.1029/96WR03137

Toro, E.F.: Shock-Capturing Methods for Free-Surface Shallow Flows. John Wiley, 2001.

Thompson, J.R., SoRenson, H.R., Gavin, H., Refsgaard, A.: Application of the coupled MIKE SHE/MIKE 11 modelling system to a lowland wet grassland in southeast England. Journal of Hydrology, 293(1-4): 151-179. 2004. http://doi.org/10.1016/j.jhydrol.2004.01.017

US Army Corps of Engineers, HEC-RAS User's Manual (version 6.4), 2023.

Van Leer, B.: Towards the ultimate conservative difference scheme V: A second order sequel to Godunov's method. Journal of Computational Physics, 32(1), 101-136, 1979. https://doi.org/10.1016/0021-9991(79)90145-1

Wing, O., Sampson, C.C., Bates, P.D., Quinn, N., Neal, J.C.: A flood inundation forecast of hurricane Harvey using a continental-scale 2D hydrodynamic model. Journal of Hydrology X, 4, 100039, 2019.

823   https://doi.org/10.1016/j.hydroa.2019.100039

824   Yu, W.: Research on Coupling Model of Hydrological and Hydraulics Based on

825   Adaptive Grid. Ph.D. Thesis, Tsinghua University, Beijing, China, 2019.

826   Xia, X., Liang, Q, Ming, X.: A full-scale fluvial flood modelling framework based on

827   a high-performance integrated hydrodynamic modelling system (HiPIMS).

828   Advances in Water Resources, 132, 103392, 2019.

829   https://doi.org/10.1016/j.advwatres.2019.103392